Journal of Engineering Science and Technology
23rd EURECA 2025 Special Issue February (2026) 95 - 109

STUDY OF ANTIFOULING PROPERTIES OF MWCNTS/GNPS NANOCOMPOSITE MEMBRANE AGAINST BSA PROTEIN

PARVINDRRA KUMARAO[1], KAH CHUN HO[1,2,3,*], JIUN HOR LOW[1,2,3], JIA LEANG TEH[1] AND YEIT HAAN TEOW[4]

[1]School of Engineering, Faculty of Innovation and Technology, Taylor's University, No. 1, Jalan Taylor's, 47500 Subang Jaya, Selangor, Malaysia
[2]Clean Technology Impact Lab, Taylor's University, No.1, Jalan Taylor's, 47500 Subang Jaya, Selangor, Malaysia
[3]Centre for Sustainable Societies, Taylor's University, No.1, Jalan Taylor's, 47500 Subang Jaya, Selangor, Malaysia
[4]Department of Chemical and Process Engineering, Faculty of Engineering and Built Environment, Universiti Kebangsaan Malaysia, 43600 UKM Bangi, Selangor , Malaysia
*Corresponding Author: kahchun.ho@taylors.edu.my

Abstract

Dairy industry generates large amount of protein-rich wastewater which requires treatment before it can be released into the environment. Despite the effectiveness of the membrane treatment, membrane fouling by the blockage of protein over membrane surface hinders its performance. The study aims to explore the use of nanocomposite membranes by direct blending multi-walled carbon nanotubes (MWCNTs) and graphene nanoplates (GNPs) into polyvinylidene fluoride (PVDF) matrix. Various ratios of MWCNTs to GNPs (0:0, 10:0, 1:4, 5:5, 3:4, 0:10) were studied at fixed nanomaterial concentration (0.1 wt%). In general, all nanocomposite membranes showed improved water permeability especially nanocomposite membrane with MWCNTs: GNP ratios of 5:5 (M3) and 0:10 (M5). In term of BSA rejection, M3 nanocomposite membrane had achieved the stable and high rejection for BSA protein (90.46-95.38%) over the two-cycle of filtration During BSA filtration, M3 nanocomposite membrane exclusively presented improved antifouling properties by normalized flux (0.8889) compared to the pristine membrane (0.3406) due to the increased pore size and highly negative surface charge. Besides, M3 nanocomposite membrane showed comparable antifouling performance under alkaline and neutral pH indicating the strong potential application for dairy wastewater with wide pH ranges.

Keywords: BSA antifouling, GNPs, MWCNTs, Nanocomposite membranes, Nanohybrid.

1. Introduction

The dairy industry in Malaysia is one of the fastest-growing industries, contributing over 1.2% of gross domestic product and bolstering the nation's economic growth [1]. The industry produces around 2 to 10 L of wastewater for every litre of milk processed [2]. The dairy wastewater contains significant levels of proteins (6-10 g/L), including bovine serum albumin (BSA), which raises the organic loads [3]. Therefore, this wastewater poses challenges to environment if untreated before discharged and protein recovery is fundamental step towards sustainable development.

Conventionally, the dairy industry wastewater is treated in three stages: removal of solids, oil, and grease, followed by removal of organic matter and nutrients, lastly polishing of the wastewater. The conventional treatment is facing great challenge by effectively addressing high concentrations of organic matter in dairy wastewater.

Membrane filtration is the recommended method for treating wastewater because it can remove impurities of diverse sizes [4]. Lakra et al. [5] reported almost complete rejection of protein (98.2%) from the dairy wastewater using ultrafiltration (UF) membrane at 1.5 bar followed by rejection of carbohydrate (65%) by forward-osmosis membrane. The recovered protein and carbohydrate from the wastewater could be used for various processes including animal feed while the treated water can be reused as process water in the dairy industry.

But of special significance is membrane fouling, which is the accumulation of particles, proteins, and microorganisms on the membrane surface that decreases the effectiveness of the membrane. Membrane cleaning such as chemical cleaning is typically conducted to restore the membrane initial permeability [6]. This resulted in increased expenditures for operation, higher cleaning expenses, and a shorter membrane lifespan [7]. Therefore, controlling protein fouling of UF membranes during their application in the dairy wastewater treatment is crucial for the efficient and low-cost operation.

Among the controlling techniques, incorporation of nanomaterials into the membrane matrix is a simple and efficient method. The presence of nanomaterials within a polymer matrix significantly enhances membrane properties like hydrophilicity, antifouling capabilities, and separation efficiency [8, 9]. Carbon-based nanomaterials have received significant attention due to their unique physicochemical properties such as excellent chemical and mechanical stability, electrical conductivity, reinforcement capability, and their antifouling properties [10-12].

Multi-walled carbon nanotubes (MWCNTs) nanocomposite membranes demonstrated superior permeability and flux recovery ratio among other carbon-based nanomaterials. For instance, Wan and Jiang [13] comparatively studied the effects of graphene oxide and MWCNTs as nanofillers in UF membranes. The addition of graphene oxide and MWCNTs at 0.5% results in enhanced surface hydrophilicity/charge, increasing the rejection of BSA (>90%). The studies also reported that MWCNT has major impact on the membrane morphological factor due to its hollow structure and the dispersion state which accelerates the formation of nanocomposite membranes.

However, MWCNTs are particularly prone to agglomeration caused by the strong van der Waals forces which makes them less favourable for large-scale application. Researchers have prepared three-dimensional hybrid fillers by mixing MWCNTs with graphene nanoplatelets (GNPs), where their π–π interactions were exploited to inhibit agglomeration and improve morphological dispersion [14]. It is reported that MWCNTs could form an extensive conjugated network that fills the gaps between GNPs nanolayers and forms conductive bridges. The nanohybrid can be used as shielding materials that attenuate the electromagnetic radiation. Besides, a 21.4% synergy rate for tensile modulus and 33.6% for Young's modulus was observed at epoxy resin when hybrid filler ratio of GNPs to MWCNTs at 1 and 0.5 wt% was added [15]. Nevertheless, up-to now, there is limited research investigating on the potential of MWCNTs/GNPs nanocomposite membranes for treating wastewater containing protein.

In this study, the relationship of MWCNTs: GNPs in the nanocomposite membranes was studied at different ratios (0:0, 10:0, 1:4, 5:5, 3:4, 0:10) and at 0.1 wt% concentration. The nanocomposite membranes were characterized in term of pore and porosity, hydrophilicity, morphology study, and surface charge. In addition, the performance of nanocomposite membranes was evaluated based on water permeability, BSA rejection and antifouling study under different pH. Membrane cleaning using distilled water was also performed to evaluate the flux recovery of the nanocomposite membranes over two-cycle of filtration.

2. Materials and Methods

2.1. Materials

Carbon nanomaterials like MWCNTs with diameter of 12-15 nm and purity >97% were supplied by Ugent Tech, Malaysia while GNPs with thickness of 2-10 nm were supplied by ACS Material, USA. Polyvinylidene Fluoride (PVDF) T-1 from Shanghai Ofluorine Co., China and dimethylacetamide (DMAc) purity 99% from Merck KGaA, Germany were used for membrane synthesis. BSA with purity of 97% and molecular weight of 66,430 Da was obtained from Solarbio, China.

2.2. Synthesis of nanocomposite membrane

MWCNTs and GNPs were blended into membrane at six various weight ratios (0:0, 10:0, 1:4, 5:5, 3:4, 0:10) as shown in Table 1. Briefly, 0.1 wt% of carbon nanomaterials were dispersed in DMAc and sonicated using ultrasonicator (P120H, Elmasonic, Germany) at a frequency of 80 kHz for 30 minutes. Next, 18 wt% of PVDF was added to the carbon nanomaterial suspension. The mixture was stirred at 250 rpm and 70℃ for 3 hours using a hotplate stirrer.

Then, the temperature was reduced to 45℃ and stirring continues for an additional 3 hours to ensure the PVDF was fully dissolves in the mixture. The membrane polymer solution was left in a desiccator overnight to remove any trapped air bubbles. Subsequently, the membrane polymer solution was casted evenly onto a flat non-woven polyester membrane support (CU414 Opti, Neenah US) which was secured to a glass plate. The glass plate with the membrane polymer solution was submerged in a 5 L distilled water for 7 hours to allow solidification. The membrane was removed from the glass plate and stored in distilled water [16].

Table 1. Membrane formulation.

Membrane Abbreviation	PVDF (wt%)	DMAC (wt%)	Weight Ratio	
			MWCNTs	GNPs
M0	18	82	0	0
M1	18	82	10	0
M2	18	82	1	4
M3	18	82	5	5
M4	18	82	3	4
M5	18	82	0	10

2.3. Membrane characterization

2.3.1. Pore and porosity

The membrane porosity was determined using the gravimetric technique and calculated using Eq. (1), while the membrane pore size was calculated using the Guerout Elford-Ferry equation (Eq. (2)). The wet membranes were soaked in distilled water for 12 hours before cutting into small pieces and weighed. Then, the wet membranes were dried for a day at 50°C in an oven before being weighed again. Finally, a micro thickness gauge was used to measure the membrane thickness. To improve the accuracy of the data, the process was repeated for three times to get average data on pore size and porosity [16].

$$\varepsilon = \frac{\frac{w_1 - w_2}{\rho_w}}{\frac{w_1 - w_2}{\rho_w} + \frac{w_2}{\rho_p}} \times 100\ \% \quad (1)$$

where ε is membrane porosity (%), w_1 and w_2 are wet and dry weight of the membrane (g), respectively, ρ_w is density of water (0.998 g/mL) and ρ_p is density of polymer (PVDF = 1.765 g/mL at 25°C), respectively [17].

$$r_m = \sqrt{\frac{(2.9 - 1.75\varepsilon)8\eta l Q}{\varepsilon \times A \times \Delta P}} \quad (2)$$

where r_m is mean of membrane pore radius, V is water flow rate in (m^3/s), η is dynamic viscosity of water at 25℃ (0.891 mPa.s), l is membrane thickness (m), ε is membrane porosity (%), P is operating pressure (Pa), A is membrane area (m^2).

2.3.2. Membrane hydrophilicity

The surface hydrophilicity of membranes was assessed by water contact measurement using a contact angle goniometer (OCA 15Pro, DataPhysics Instruments, Germany) via the sessile drop method. Around 4 μL of water droplet was gently dispensed on the membrane surface and at least three measurements were conducted to obtain an average value.

2.3.3. Morphology study

The top surface and cross-sectional morphologies of the membranes were examined by using Scanning Electron Microscope (Hitachi TM3000, Tokyo, Japan) at magnification of 1000× and 15.0 kV. To examine the surface morphology, a membrane sample of 0.5 cm × 0.5 cm was cut and observed. For

cross-sectional morphologies, membrane samples were submerged in liquid nitrogen and snapped to obtain clean cross-section view.

2.3.4. Surface charge

The membrane surface charge was determined by using zeta potential analyser (SurPASS 3, Anton Paar GmbH, Austria). The membrane sample was mounted on sample holder and pH of electrolyte solutions was adjusted from 3 to 11.

2.4. Membrane performance

A 10-L crossflow filtration system was utilized to evaluate the performance of membrane permeability, BSA rejection and antifouling. To perform the experiment, the membranes were cut into a disc shaped with effective filtration area of 14.5 cm^2 [18].

2.4.1. Permeability

To minimize the impact of compaction, the membrane was compressed for 30 minutes at a constant pressure of 3 bar prior to the membrane permeability test. For membrane permeability, distilled water was filtered through the membrane for 10 minutes at different transmembrane pressures (TMPs) of 1.0, 1.5 and 2.0 bar. The amount of permeate collected was then measured and permeate flux is determined using Eq. (3). The membrane permeability was obtained as the gradient of permeate flux against TMPs.

$$J = \frac{\Delta V}{A\Delta t} \tag{3}$$

where J is permeate flux ($Lm^{-2}h^{-1}$), ΔV is permeate volume (L), A is effective surface area (m^2) and Δt is permeation time (h).

2.4.2. BSA rejection and antifouling performance

500 ppm BSA solution was used as the feed solution and filtered through the membranes at 2 bars. Membranes were gently cleaned by distilled water for 1 minute after 30 minutes of filtration [19, 20]. Then, the membranes were filtered through BSA solution for another 30 minutes. The concentration of BSA in the permeate was measured using UV/VIS spectrophotometer (Spectroquant® Prove 300, Merck, Germany) at wavenumber of 278 nm [21]. BSA rejection efficiency (R) was evaluated according to Eq. (4).

$$R(\%) = \left(\frac{C_F - C_P}{C_F}\right) \times 100 \tag{4}$$

where the variables C_P and C_F represent the concentrations of BSA in the permeate and feed, respectively, measured in ppm [22].

The fouling behaviour of the membranes was evaluated by monitoring the normalized flux over the two-cycle filtration using Eq. (5). Additionally, the antifouling performance of membrane was investigated at various pH of BSA solution of pH 4 and pH 12 adjusted using HCl and NaOH aqueous solution.

$$Normalized\ flux = \frac{J_1}{J} \tag{5}$$

where J_1 is BSA flux and J is distilled water flux.

3. Results and Discussion

3.1. Membrane characterization

Table 2 shows the porosity and mean pore size of the synthesized membranes. As seen, the addition of pristine carbon nanofillers like MWCNTs and GNPs reduced the membrane porosity particularly at high GNP weightage with porosity reduction up to 18.94%. This is due to the planar nature of GNPs tend to self-adjust their basal planes during the membrane phase inversion, thus creating a compact packing membrane structure. Similar result was also reported that membrane porosity decreased by 3% with the addition of the GNPs in the polyethersulfone and PVDF using electrospinning method due to the attraction forces between the GNPs resulting in multilayer layer and a more compact membrane [23].

In terms of pore size, the nanocomposite membranes show significant increase in pore size by 43.53-123.78%. This is also consistent with the addition of graphene oxide and carboxylic-functionalized carbon nanotube which affects the formation kinetics of membranes leading to the larger surface pores [13].

Larger pore size up to 15-43 nm and 16-54 nm was observed for graphene oxide and carboxylic-functionalized carbon nanotube nanocomposite membrane as compared to the pristine membrane (14-21 nm). Additionally, the nanocomposite membranes with nanohybrid of MWCNTs: GNP (M2, M3 and M4) exhibited higher increment membrane pore size (65.90-123.78%) as compared to the pristine MWCNTs and GNP nanocomposite membranes (43.53-90.04%). This can be explained by the improved dispersion of MWCNTs/GNPs in the membrane matrix and created "tortuous path" with a better barrier effect for water filtration [24].

Table 2. Porosity and mean pore radius of membrane.

Membrane	Porosity, ε (%)	Mean pore radius, rm (nm)
M0	45.67 ± 8.36	17.10 ± 2.05
M1	42.32 ± 1.23	24.54 ± 0.48
M2	35.58 ± 4.93	28.37 ± 2.61
M3	36.68 ± 7.44	38.26 ± 5.28
M4	40.89 ± 13.11	30.14 ± 7.43
M5	26.73 ± 2.97	32.50 ± 2.21

Figure 1 shows the membrane surface hydrophilicity measured by water contact angle. As seen, the pristine PVDF membrane (M0) has a contact angle of 80.17° indicating its intrinsic hydrophobic nature [25]. The addition of MWCNTs decreases the contact angle of nanocomposite membrane (M1) to 76.87° as the pristine MWCNTs may contain minute number of hydrophilic groups which might play a favourable role in elevating the membrane water permeability [26].

In contrast, the nanocomposite membranes with the presence of GNPs showed increased of contact angle with the highest contact angle (89.71°) achieved by MWCNTs: GNP ratio of 3:4. This could be due to the hydrophobic nature of multi-layer graphene sheets in platelet shape though the edges of the graphene sheets may contain oxygenated-based functional groups [27].

3.2. Membrane performance

3.2.1. Permeability

Figure 2 shows the membrane water permeability where most of the nanocomposite membranes have the similar permeability as the pristine membrane (29.65-36.57 L/m^2·h·bar) except for M1, M3 and M5 nanocomposite membranes. Particularly, M3 nanocomposite membrane shows the highest water permeability of 105.60 L/m^2·h·bar which is 252.6% higher compared to the pristine M0 membrane. This can be explained by the significant increment of membrane pore size as presented in Table 2.

Larger membrane pores led to the lower hydraulic transport resistance hence higher water permeance despite marginal decrease in the membrane porosity after the addition of MWCNTs and GNPs (5:5). This indicates the membrane pore size has more significant effect on membrane permeability compared to the membrane porosity. This is in accordance with Morsi et al. [28] where considerably higher water permeability (62 L/m^2·h·bar) was attained by membrane with larger pore diameter (0.04 μm) compared to the that of membrane (23 L/m^2·h·bar) with relatively smaller pore diameter (0.017 μm) despite similar porosity (76-80%).

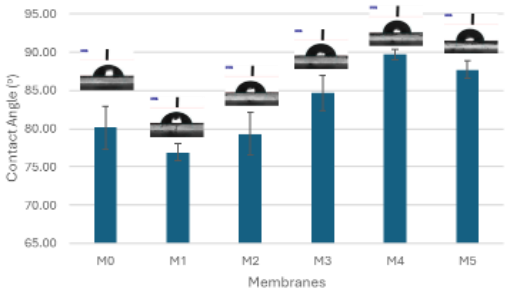

Fig. 1. Membrane hydrophilicity.

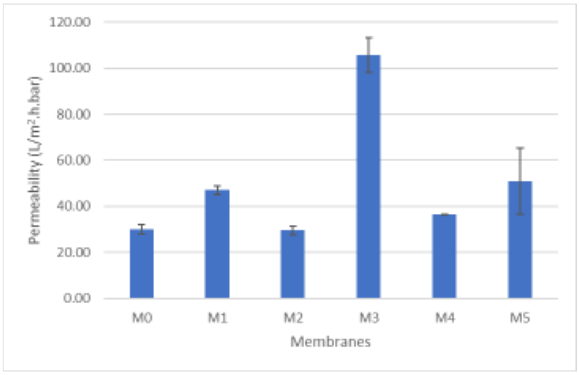

Fig. 2. Permeability of membrane.

This is also evidenced by the nanocomposite membrane (M1, M3 and M5) top surface and cross-sectional images shown in Fig. 3. As shown, Both M1 and M3 nanocomposite membranes presented a more porous membrane surface (Fig. 3(a)

and (b)) as compared to the M5 nanocomposite membrane (Fig. 3(c)) represented by the dark spot. This is due to the planar nature of GNPs created a dense membrane structure in M5 nanocomposite membrane [29]. In M5 nanocomposite membrane. In term of cross-sectional images, M3 nanocomposite membrane showed a thinner skin layer with present large and irregular cavities (Fig. 3(e)) while M1 and M5 nanocomposite membrane (Fig. 3(d) and (f)) presented a thicker skin layer with reduced tortuosity on the membrane support. Combining both porous membrane surface and large void cavities, M3 nanocomposite membrane allowed water molecules to penetrate easily and expected to maintain high pollutant rejection.

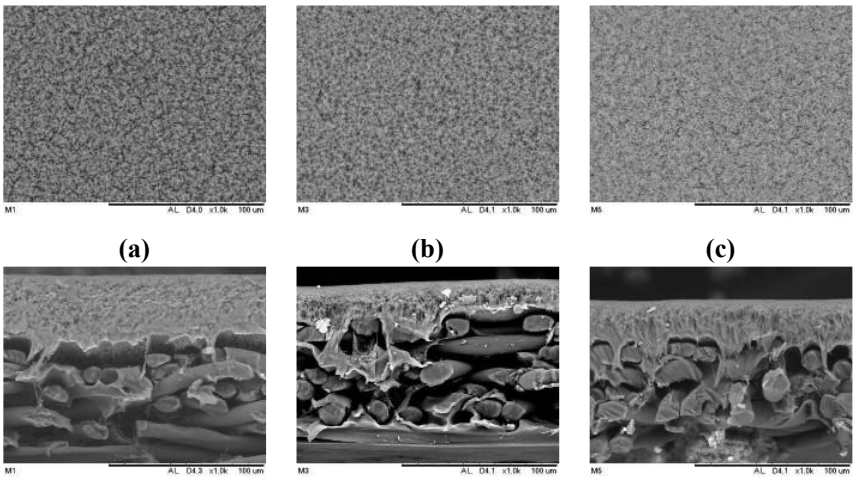

Fig. 3. Membrane morphology.

3.2.2. BSA rejection

Figure 4 depicts the BSA rejection of membranes over the two-cycle of BSA filtration. In general, the membrane BSA rejection ranges from 86.09-98.35% in the first filtration cycle. The high BSA rejection is primarily controlled by membranes pore size as reported in Table 2. According to Saleem and Al-Jubouri [30], membranes produced using 18 wt% PVDF and 6 wt% PEG has a molecular weight cut-off of 478 Da using various dyes such as RhB, acid orange 10 and congo red. As such, the BSA with higher MW (66,430 Da) used in this study will retain on the membrane surface governed by sieving mechanism.

Figure 5 illustrates the membrane surface charge determined using zeta potential analyser. The isoelectric points of M1, M3 and M5 nanocomposite membranes are 4.36, 3.99, and 4.22, respectively. As seen, the M1, M3 and M5 nanocomposite membranes exhibit similar negative surface charge (-22.24 mV to -20.66 mV) at neutral pH. Hence, it creates electrorepulsive force between the membrane surface and negatively charged BSA, thereby increased the BSA rejection efficiency [31].

After membrane cleaning with distilled water, the BSA rejection decreased to 66.96-90.46% in the second filtration cycle. This could be due to presence of BSA residues on the membrane surface or pores after water cleaning. This could

potentially saturate the membrane structure leading to the leaching of BSA through membrane [32].

Besides, marginally decrease in BSA rejection is observed for M2 and M3 nanocomposite membrane (4.92-6.48%) as compared to that of M4 and M5 nanocomposite membrane (19.13-19.28%). This indicates that the stability of M2 and M3 nanocomposite membranes in filtration cycles with minimum loss.

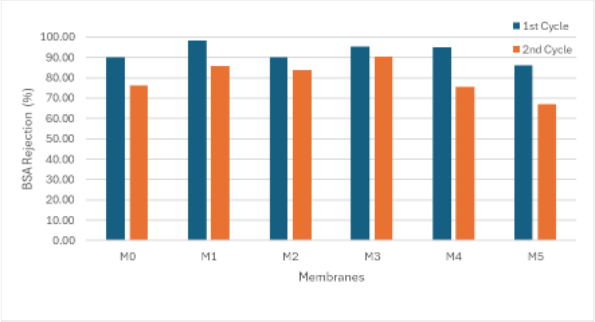

Fig. 4. BSA rejection of membrane.

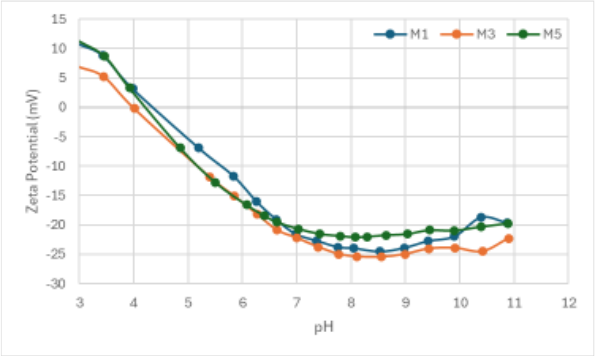

Fig. 5. Membrane surface charge.

3.2.3. Antifouling

Figure 6 shows the normalized flux of membranes over the two-cycle of BSA filtration at 2 bars. As shown, in the first cycle, the highest normalized flux is attained by M3 nanocomposite membrane (0.8899) while the lowest normalized flux is attained by M0, M4, and M5 nanocomposite membranes (0.3406-0.4444).This can be explained by the hydrophilicity of membrane surface as presented in Fig. 1.

The fouling of BSA is influenced by hydrophobic interactions, causing hydrophobic BSA to adsorb more readily onto hydrophobic membrane surfaces. Rajabzadeh et al. [33] investigated the hydrophilic interactions between the BSA, and membrane surface grafted with hydrophilic zwitterion chains. It is reported that the grafted membrane with higher hydrophilicity exhibited considerable antifouling property when it was exposed to BSA. This is due to the formation of water layer

on the membrane surface and inhibited hydrophobic-hydrophobic interaction between membrane and BSA.

For M3 nanocomposite membrane, though the membrane is considerably less hydrophobic, the nanocomposite membrane has the biggest pore size allowing the BSA and water solute to pass through the membrane easily hence reducing the fouling propensity. This can be evidenced by the slow fouling rate as shown in the Fig. 5. Jeon et al. [34] reported the development of membrane fouling on PVDF membranes decreased in the order membrane pore size 0.02 > 0.25 > 0.4 μm. However, it should be noted that membrane fouling can be affected by complicated factors such as surface chemical properties, surface morphology, pore size, hydrophilic/phobic properties, and solution chemistry [35].

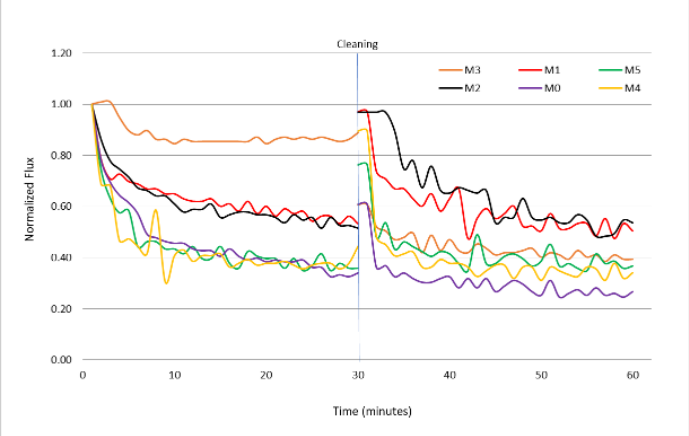

Fig. 6. Membrane normalized flux against time.

Upon membrane cleaning, most of the membrane flux recovered in the range of 78.72-113.16% with respect to the initial membrane flux. This is because the distilled water dislodged the blockage of BSA solute on the membrane surface and some within the pores. M1 and M2 nanocomposite membranes demonstrated excellent cleaning efficiency with almost complete flux recovery (96.48-97.09%). This can be explained by the hydrophilic membrane surface shown in Fig. 1.

The hydrophilic membrane surface provides a repulsive and hydrated layer resisting significant adhesion of most hydrophobic components. Hence, simple water cleaning is able to disrupt the BSA adhesions [36]. However, it is worth to note that the normalized flux of M3 nanocomposite membrane remains low despite membrane cleaning. The normalized flux of M3 nanocomposite membrane after cleaning is unexpectedly lower (0.6068) compared to the end of first cycle (0.8889). This supports our assumption that the large membrane pores allow the penetration of BSA into the pore structure. Hence, this causes BSA remained trapped within the pores and could not effectively removed by hydraulic cleaning.

As M3 nanocomposite membrane demonstrates excellent performance in terms of water permeability and stable BSA rejection, further investigation on antifouling performance of M3 membrane was conducted using BSA solution at alkaline (pH 12) and acid (pH 4) condition. This study is important due to the pH variation of dairy

wastewater by the use of acid, alkaline cleaners and sanitizers in the industry. Figure 7 illustrates the normalized flux of M3 nanocomposite membranes under various pH of BSA over two-cycle of filtration. As seen, the normalized flux of M3 nanocomposite membrane for neutral and alkaline condition is almost identical in the range of 0.7088-0.8889 which is significantly higher compared to the acidic condition (0.4978).

This can be explained by the M3 nanocomposite membrane surface charge at various pH in Fig. 5. At high pH, the membrane surface is more negatively charge and this increased the electrical repulsion force between the membrane surface and BSA [37]. Therefore, the charge repulsion mitigates the attachment of BSA on the membrane surface and reduce the fouling propensity. On the contrary, at low pH, the BSA tends to attract to the positively charged membrane surface because they are oppositely charged, thus leading to rapid membrane flux decline.

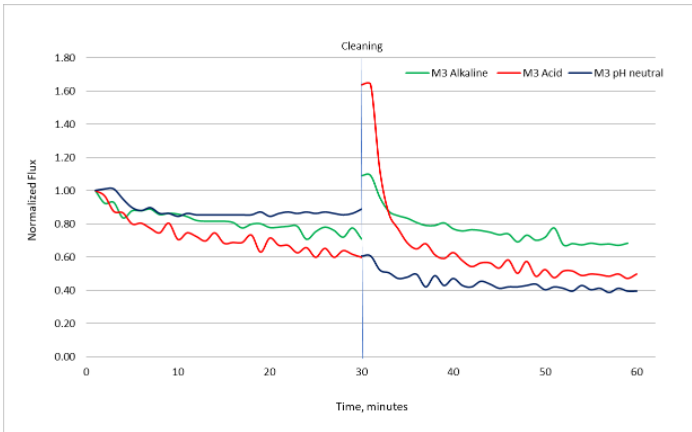

Fig. 7. Normalized flux of M3 nanocomposite membrane under various pH of BSA.

Likewise, upon membrane cleaning using distilled water, the flux of M3 nanocomposite membrane is recovered by 53.57% and 228.57%, respectively at alkaline (pH 12) and acidic (pH 4) BSA solution as compared to the poor recovery at neutral pH (-31.73%). During alkaline BSA filtration, the negatively charged BSA was loosely bound to the negatively charged membrane surface. The BSA solute can be removed easily through water rinsing resulted in almost 100% flux recovery with respect to the initial water flux. Although higher flux recovery was observed at acidic BSA filtration, it is believed that the structure of membrane has been compromised by the harsh chemicals. Similar result is reported by Lasisi et al. [38] who studied the effect of sulfuric acid on the chemical, mechanical and physical properties of PVDF membrane after prolonged exposure time. It is reported that the intense degradation of the membranes structure via pore enlargement. This is due to the protonation effect caused by the sulfuric acid attack on the membranes surface. However, conflicting observation is reported where the most severe effect is found for the membranes treated with alkaline solution, then hypochlorite and acid solution [39]. Hence, further research should be conducted to examine the membrane stability by different cleaning conditions such as chemicals, temperature and cleaning period.

4. Conclusion

To sum up, this research investigated the integration of MWCNTs and GNPs nanomaterials affecting the structural and functional properties of nanocomposite membranes. Through a thorough examination of the synthesized membranes, the study also seeks to understand their characteristics and how well they treat BSA protein, which is a byproduct of the dairy industry's wastewater, with the ultimate objective of maximizing their performance for practical uses. The integration of MWCNTs and GNPs into the membrane matrix enhanced its hydrophilicity and significantly increased membrane pore size compared to the pristine PVDF membrane (M0). This structural modification allows water molecules to pass through more easily while maintaining effective rejection of BSA solute.

In particular, the M3 nanocomposite membrane, which contains an optimal 5:5 ratio of MWCNTs to GNPs, exhibited the highest water permeability among all tested membranes. The balanced distribution of nanofillers in the membrane not only prevents aggregation but also creates a more interconnected pore network, enabling faster water transport without compromising selectivity. The combination of increased pore size and improved surface charge is the key factor behind the superior filtration performance.

Besides, the normalized flux of M3 nanocomposite membrane for neutral and alkaline condition is almost comparable in the range of 0.7088-0.8889 which is significantly higher compared to the acidic condition. Upon membrane cleaning, the membrane flux is recovered significantly (53.57%) at alkaline condition without compromising the membrane structure at alkaline condition. Further research should be conducted to examine the membrane stability by different cleaning conditions such as chemicals, temperature and cleaning period using the real dairy industry wastewater.

Acknowledgements

The authors wish to gratefully acknowledge the financial support by Taylor’s University through Taylor’s Internal Research Grant Scheme - Impact Lab Grant (TIRGS-ILG) (Project Code: TIRGS-ILG/2/2024/SOE/001).

References

1. Ali, A.; and Haseeb, M. (2019). Radio frequency identification (RFID) technology as a strategic tool towards higher performance of supply chain operations in textile and apparel industry of Malaysia. *Uncertain Supply Chain Management*, 7(2), 215-226.
2. Custodio, M.; Peñaloza, R.; Espinoza, C.; Espinoza, W.; and Mezarina, J. (2022). Treatment of dairy industry wastewater using bacterial biomass isolated from eutrophic lake sediments for the production of agricultural water. *Bioresource Technology Reports*, 17, 100891.
3. Aani, S.A.; Mustafa, T.N.; and Hilal, N. (2020). Ultrafiltration membranes for wastewater and water process engineering: A comprehensive statistical review over the past decade. *Journal of Water Process Engineering*, 35, 101241.
4. Tan, Y.H.; Lau, W.J.; Goh, P.S.; Yusof, N.; and Ismail, A.F. (2018). Nanofiltration of aerobically-treated palm oil mill effluent: Characterization of

the size of colour compounds using synthetic dyes and polyethylene glycols. *Journal of Engineering Science and Technology*, 13(1), 1-10.

5. Lakra, R.; Choudhury, S.; and Basu, S. (2021). Recovery of protein and carbohydrate from dairy wastewater using ultrafiltration and forward osmosis processes. *Materials Today*: *Proceedings*, 47, 1400-1403.
6. Luján-Facundo, M.J.; Mendoza-Roca, J.A.; Cuartas-Uribe, B.; and Álvarez-Blanco, S. (2016). Study of membrane cleaning with and without ultrasounds application after fouling with three model dairy solutions. *Food and Bioproducts Processing*, 100, 36-46.
7. Mohammad, A.W.; Teow, Y.H.; Ho, K.C.; and Rosnan, N.A. (2018). Recent developments in nanofiltration for food applications. *Nanomaterials for Food Applications*, 101-120.
8. Tai, V.C.; Che, H.X.; Kong, X.Y.; Ho, K.C.; and Ng, W.M. (2023). Decoding iron oxide nanoparticles from design and development to real world application in water remediation. *Journal of Industrial and Engineering Chemistry*, 127, 82-100.
9. Nik-Abdul-Ghani, N.-R.; Jami, M.S.; Engliman, N.-S.; Amosa, M.K.; and Isa, M.H. (2021). Study of graphene oxide-polymer nanocomposite (GPN) adsorptive membrane for lead removal from wastewater. *Journal of Engineering Science and Technology*, 16(5), 3620-3636.
10. Noamani, S.; Niroomand, S.; Rastgar, M.; and Sadrzadeh, M. (2019). Carbon-based polymer nanocomposite membranes for oily wastewater treatment. *NPJ Clean Water*, 2(1), 20.
11. Vaka, M.; Walvekar, R.; Khalid, M.; Jagadish, P.; and Low, J.H. (2021). Corrosion, rheology, and thermal ageing behaviour of the eutectic salt-based graphene hybrid nanofluid for high-temperature TES applications. *Journal of Molecular Liquids*, 334, 116156.
12. Cheong, K.L. et al. (2024). Graphene nanoplatelets/polylactic acid conductive polymer composites: Tensile, thermal and electrical properties. *Chemical Engineering & Technology*, 47(11), e202300592.
13. Wan, Z.; and Jiang, Y. (2021). Synthesis-structure-performance relationships of nanocomposite polymeric ultrafiltration membranes: A comparative study of two carbon nanofillers. *Journal of Membrane Science*, 620, 118847.
14. Lin, C.-L. et al. (2022). Graphene nanoplatelet/multiwalled carbon nanotube/polypyrrole hybrid fillers in polyurethane nanohybrids with 3D conductive networks for EMI shielding. *ACS Omega*, 7(49), 45697-45707.
15. Odedairo, T. et al. (2014). One-pot synthesis of carbon nanotube–graphene hybrids via syngas production. *Journal of Materials Chemistry A*, 2(5), 1418-1428.
16. Chun, H.K. (2019). *Graphene oxide*/*carbon nanotubes conductive membrane with active antifouling properties*. PhD Thesis, Universiti Kebangsaan, Malaysia.
17. Ho, K.C.; Raffi, S.M.; and Teow, Y.H. (2022). Synthesis of MWCNTs/TiO2 photocatalytic nanocomposite membrane via in-situ colloidal precipitation method for methyl orange removal. *International Journal of Nanoelectronics and Materials*, 15(3), 207-222.

18. Li, Q.; Reeve, C.; Martinez, L.; and Wright, S. (2019). *Scale-up in biotechnology*. In Li, Q.; Reeve, C.; Martinez, L.; and Wright, S. (Eds.), *Comprehensive Biotechnology*. Elsevier, 919-932.
19. Haan, T.Y.; Ghani, M.S.H.; and Mohammad, A.W. (2018). Physical and chemical cleaning for nanofiltration/reverse osmosis (NF/RO) membranes in treatment of tertiary palm oil mill effluent (POME) for water reclamation. *Jurnal Kejuruteraan*, SI1(4), 51-58.
20. Farjami, M.; Vatanpour, V.; and Moghadassi, A. (2020). Fabrication of a new emulsion polyvinyl chloride (EPVC) nanocomposite ultrafiltration membrane modified by para-hydroxybenzoate alumoxane (PHBA) additive to improve permeability and antifouling performance. *Chemical Engineering Research and Design*, 153, 8-20.
21. Pishnamazi, M. et al. (2020). Metal organic framework nanoparticles loaded-PVDF/chitosan nanofibrous ultrafiltration membranes for the removal of BSA protein and Cr(VI) ions. *Journal of Molecular Liquids*, 317, 113934.
22. Zhang, J. et al. (2023). Ag@BiOBr/PVDF photocatalytic membrane for remarkable BSA anti-fouling performance and insight of mechanism. *Journal of Membrane Science*, 677, 121611.
23. Salem, M.S.; El-Shazly, A.H.; Nady, N.; Elmarghany, M.R.; and Sabry, M.N. (2019). PES/PVDF blend membrane and its composite with graphene nanoplates: Preparation, characterization, and water desalination via membrane distillation. *Desalination and Water Treatment*, 166, 9-23.
24. Zhuo, D. et al. (2013). Flame retardancy effects of graphene nanoplatelet/carbon nanotube hybrid membranes on carbon fiber reinforced epoxy composites. *Journal of Nanomaterials*, 2013(1), 820901.
25. Lee, C.Z.; Chun, H.K.; Chan, M.K.; and Teow, Y.H. (2022). Effect of carbon nanomaterials concentration in nanocomposite membrane for methyl blue dye removal. *Jurnal Teknologi*, 84(6), 19-27.
26. Ma, J. et al. (2013). Role of oxygen-containing groups on MWCNTs in enhanced separation and permeability performance for PVDF hybrid ultrafiltration membranes. *Desalination*, 320, 1-9.
27. Lim, C.S.; Kueh, T.C.; Soh, A.K.; and Hung, Y.M. (2020). Engineered superhydrophilicity and superhydrophobicity of graphene-nanoplatelet coatings via thermal treatment. *Powder Technology*, 364, 88-97.
28. Morsi, R.E. et al. (2023). Influence of the fabrication conditions on the physical properties and water treatment efficiency of cellulose acetate porous membranes. *Water*, 15(6), 1061.
29. Fadaie, N. et al. (2021). Novel plasma functionalized graphene nanoplatelets (GNPs) incorporated in forward osmosis substrate with improved performance and tensile strength. *Journal of Environmental Chemical Engineering*, 9(4), 105708.
30. Saleem, A.G.; and Al-Jubouri, S.M. (2024). Separation performance of cationic and anionic dyes from water using polyvinylidene fluoride-based ultrafiltration membrane incorporating polyethylene glycol. *Desalination and Water Treatment*, 319, 100546.
31. Chang, Z.H.; Sum, J.Y.; Leow, L.H.T.; Teow, Y.H.; and Yeap, S.P. (2025). Interfacial interaction energy and pore blockage analysis of protein fouling in ultrafiltration-like forward osmosis. *Applied Surface Science*, 693, 162787.

32. Manios, T.K.; Mattia, D.; and Bird, M.R. (2023). The influence of multiple fouling and cleaning cycles upon the performance of polyethersulphone membrane filters during coffee extract decaffeination. *Food and Bioproducts Processing*, 140, 1-15.
33. Rajabzadeh, S. et al. (2020). Effect of hydrophilic-hydrophilic interactions between the foulant and membrane surface on the fouling propensity of different foulants. *Journal of Membrane Science and Research*, 6(4), 383-389.
34. Jeon, S. et al. (2016). The effect of membrane material and surface pore size on the fouling properties of submerged membranes. *Water*, 8(12), 602.
35. Chen, Y.M.; Ho, K.C.; Chan, M.K.; Teow, Y.H.; and Idris, A.I.M (2022). Optimization of antifouling properties of mixed matrix membrane synthesized via in-situ colloidal precipitation. *Journal of Membrane Science and Research*, 9(1), e254998.
36. Li, X.; Cai, T.; Amy, G.L.; and Chung, T.-S. (2017). Cleaning strategies and membrane flux recovery on anti-fouling membranes for pressure retarded osmosis. *Journal of Membrane Science*, 522, 116-123.
37. Aminudin, N.N.; Basri, H.; Yunos, M.Z.; Harun, Z.; and Sean, G.P. (2014). Effect of pH on bovine serum albumin (BSA) solution to polysulfone-based membrane. *Jurnal Teknologi*, 70(2).
38. Lasisi, K.H. et al. (2020). Impacts of sulfuric acid on the stability and separation performance of polymeric PVDF-based membranes at mild and high concentrations: An experimental study. *Membranes*, 10(12), 375.
39. Lang, W.-Z. et al. (2014). The contrastive study of chemical treatment on the properties of PVDF/PFSA and PVDF/PVP ultrafiltration membranes. *Desalination*, 341, 72-82.